J Eng Math (2021) 131:8
https://doi.org/10.1007/s10665-021-10177-5

Charging of flowable electrodes with bimodal distribution of carbon particles

Brandon Stacks · Haoxiang Luo · Deyu Li

Received: 28 January 2021 / Accepted: 28 July 2021 / Published online: 23 October 2021

Abstract Carbon slurries as "flowable electrodes" have been used recently in a few electrochemical systems, e.g., electrochemical flow capacitors (EFCs) for energy storage and flow-electrode capacitive deionization (FCDI) for water treatment. These slurries typically have three parts: activated carbon particles, a conductive additive such as carbon black, and an aqueous electrolyte solution. Previously, a particle-based computational model that employs Stokesian dynamics was developed to describe the particle motion and interaction, while simultaneously solving for the charge transfer inside an electrical network of moving particles. In this work, we develop a unified expression of the dynamically varying electrical network. Furthermore, we incorporate a group of smaller particles as the conductive additive, whose effect on the charge transfer of the slurry is studied. The results suggest that at lower concentrations, the small particles may enhance charge transfer by filling interstitial spaces and bridging contacts of large particles; however, at higher concentrations, the benefits are not as clear since direct contacts of the large particles play the dominant role in charge transfer.

Keywords Bimodal distribution · Charge model · Electrochemical flow capacitors · Energy storage · Flow-electrode capacitive deionization · Flowable electrodes · Stokesian dynamics

1 Introduction

Activated carbon particles submerged in an aqueous electrolyte to form a slurry have shown to be useful as "flowable electrodes" in a few emerging electrochemical systems, such as the electrochemical flow capacitor (EFC) [1–3] and flow-electrode capacitive deionization (FCDI) [3–5]. These systems employ the supercapacitive properties of activated carbon for high power density charging and discharging. Furthermore, the carbon slurry is flowable to allow for continuous operation of the charging-discharging cycle. For example, during the charging cycle in an EFC, the uncharged slurry is pumped through the EFC cell, which is a channel that has been divided in half by a non-conducting permeable membrane separator that allows ionic exchange between the two chambers (see Fig. 1a). The ions in the electrolyte are attracted to the vicinity of the available pores of the activated carbon particles to form

B. Stacks · H. Luo (✉) · D. Li
Department of Mechanical Engineering, Vanderbilt University, Nashville, TN 37235, USA
e-mail: haoxiang.luo@vanderbilt.edu

D. Li
e-mail: deyu.li@Vanderbilt.Edu

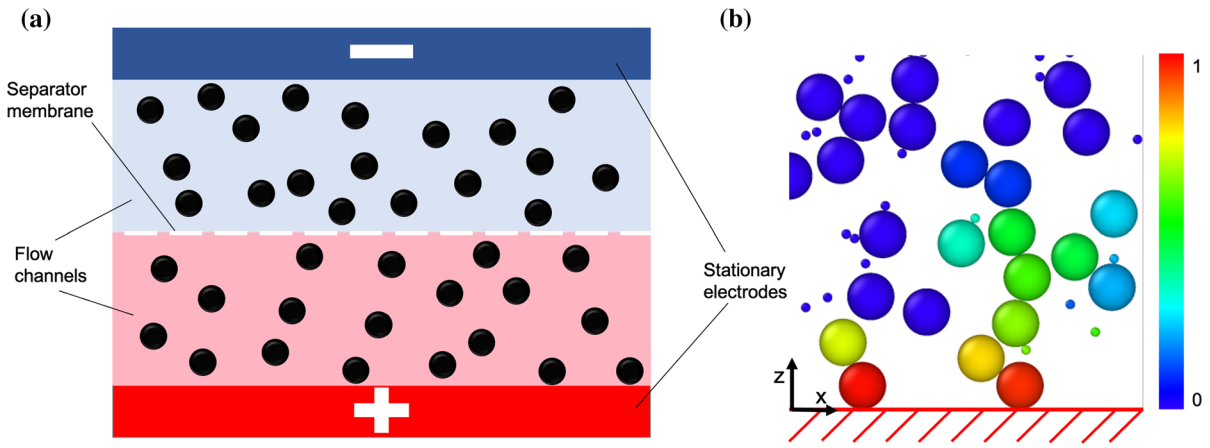

Fig. 1 **a** A diagram showing the double channel through which the carbon-electrolyte slurry flows. **b** A computational model of the carbon spheres coupling the hydrodynamic interactions and the charge transfer from the wall (stationary electrode) to the particles, where color bar represents the charge level

electric double layers (EDL) within the pores. At the same time, electrons are passed from a stationary electrode to the carbon particles via electrode–particle and particle–particle interactions. To discharge the device, the slurry is pumped back through the device where the ions are released and electrons are supplied to a load in a reversed path through the particle–particle and electrode–particle interactions. Therefore, these interactions are crucial to the effectiveness of the EFC.

In the past, the slurry electrode has been modeled as a lumped-parameter resistor-capacitor (RC) circuit for the charging cell [2] and also a single-phase, continuum-based material to describe advection-diffusion of the ions and inhomogeneous distribution of the electrical charges stored in the slurry [6,7]. While these models provide helpful insight at the system level, they do not provide information into how the particle interactions affect the charging capabilities of the slurry. At the particle level, the dynamic behavior of the clusters essentially leads to a random and topology-varying network for electronic percolation through the slurry. In a recent study by Karzar-Jeddi et al. [8], a particle-based computational model was developed to address the coupling between the particle motion and the charge transfer. Specifically, in this study, Stokesian dynamics (SD) was used to simulate the microhydrodynamics of the particles' clustering behavior, and a generalized electrical circuit at the particle level was developed to solve the charge transfer among the particles. This generalized circuit model incorporates the effects of the dynamic circuit configuration due to random motion of the particles with respect to one another, and it simulates charging and discharging of individual particles during interaction. Although there has been significant modeling work in the area of electrochemical batteries that has to do with particle-based porous materials, e.g., single-particle models and many-particle models [9,10], the computational model in Karzar-Jeddi et al. [8] (also considered in the present study) is distinct from those respective electrode models in that the flowable electrode involves hydrodynamic interactions and re-configuration of moving particles. For simplification, each particle in Karzar-Jeddi et al. [8] is reduced to a simple resistor-capacitor circuit without considering the detailed diffusion process inside the particle. That study also investigated the statistics of the micro-structures for a monodisperse slurry. Furthermore, the model was validated against the macroscopic charging behavior of the moving slurry measured in the EFC experiment.

In this work, we will extend the particle-level circuit model in that study [8] and develop a unified expression of its charging dynamics. Furthermore, we will use this model to study the effect of the conductive additive (here carbon black is considered) by incorporating the additive as smaller particles than the charge-carrying activated carbon. Their motion and interaction with the activated carbon particles will be solved simultaneously in a Stokesian dynamics simulation. The formulation of the theoretical model, simulation setup, results and brief discussions are described in the following sections.

2 Theoretical formulations

In the slurry electrode, the channel sizes are typically small (only a few millimeters) [1,2], and the Reynolds number is low. The flow can thus be treated as Stokes flow. We use Stokesian dynamics [11,12] to calculate the particle mobility. In a recent work [13], the authors have derived the theoretical formulation for the mobility of polydisperse spherical particles near a flat no-slip wall, and the formulation was implemented in a Stokesian dynamics code that will be used here for the bimodal configuration. We consider a single slice of the slurry electrode under shear condition as shown in Fig. 1b. The particles are assumed to be rigid and spherical. The larger particles represent activated carbon beads in several previous studies of the EFC [1–3], and the smaller particles represent the carbon black as the conductive additive, which does not have a porous structure and thus has little capacitance. We first briefly summarize the Stokesian dynamics model and will then describe the charge transport model.

It is important to note that in this study, we only consider the hydrodynamic interactions of the particles. A previous work from our group [8] discussed the scaling of other possible interactions such as gravity, Brownian motion, van der Waals, and double layer forces. Most of those forces can be neglected for the particle size between 1 and 20 μm. For example, the gravitational force is less than 10% of the drag force in this size range. The Brownian motion is two orders of magnitude lower than the flow velocity even for particles of 1 μm diameter moving at 0.1 mm/s. The Debye length is on order of nm and is even smaller than the particle surface roughness, and thus, the double layer forces can be ignored as well. Depending on the separation gap, the scaling analysis suggests there might be a van der Waals effect present. Future experimental study on direct observation of the particle interactions will likely provide complementary information how significant the van der Waals force is in the flowable electrode.

2.1 Hydrodynamic interactions

For a specific configuration of N particles in the Stokes flow limit, its hydrodynamics is governed by a linear equation system. That is, the translational velocity $\mathbf{U}$, the rotational velocity Ω, and the strain rate $\mathbf{E}$, are linearly proportional to the external force $\mathbf{F}$, the external torque $\mathbf{L}$, and the stresslet $\mathbf{S}$ on the particle through the grand mobility matrix $\mathcal{M}$. The equation reads [14,15]

$$\begin{pmatrix} \mathbf{U}^{\alpha} - \mathbf{U}^{\infty}(\mathbf{x}^{\alpha}) \\ \mathbf{U}^{\beta} - \mathbf{U}^{\infty}(\mathbf{x}^{\beta}) \\ \vdots \\ \boldsymbol{\Omega}^{\alpha} - \boldsymbol{\Omega}^{\infty}(\mathbf{x}^{\alpha}) \\ \boldsymbol{\Omega}^{\beta} - \boldsymbol{\Omega}^{\infty}(\mathbf{x}^{\beta}) \\ \vdots \\ -\mathbf{E}^{\infty}(\mathbf{x}^{\alpha}) \\ -\mathbf{E}^{\infty}(\mathbf{x}^{\beta}) \\ \vdots \end{pmatrix} = \begin{pmatrix} \mathbf{M}_{\mathrm{UF}}^{\alpha\alpha} & \mathbf{M}_{\mathrm{UF}}^{\alpha\beta} & \cdots & \mathbf{M}_{\mathrm{UL}}^{\alpha\alpha} & \mathbf{M}_{\mathrm{UL}}^{\alpha\beta} & \cdots & \mathbf{M}_{\mathrm{US}}^{\alpha\alpha} & \mathbf{M}_{\mathrm{US}}^{\alpha\beta} & \cdots \\ \mathbf{M}_{\mathrm{UF}}^{\beta\alpha} & \mathbf{M}_{\mathrm{UF}}^{\beta\beta} & \cdots & \mathbf{M}_{\mathrm{UL}}^{\beta\alpha} & \mathbf{M}_{\mathrm{UL}}^{\beta\beta} & \cdots & \mathbf{M}_{\mathrm{US}}^{\beta\alpha} & \mathbf{M}_{\mathrm{US}}^{\beta\beta} & \cdots \\ \vdots & \vdots & & \vdots & \vdots & & \vdots & \vdots & \\ \mathbf{M}_{\Omega\mathrm{F}}^{\alpha\alpha} & \mathbf{M}_{\Omega\mathrm{F}}^{\alpha\beta} & \cdots & \mathbf{M}_{\Omega\mathrm{L}}^{\alpha\alpha} & \mathbf{M}_{\Omega\mathrm{L}}^{\alpha\beta} & \cdots & \mathbf{M}_{\Omega\mathrm{S}}^{\alpha\alpha} & \mathbf{M}_{\Omega\mathrm{S}}^{\alpha\beta} & \cdots \\ \mathbf{M}_{\Omega\mathrm{F}}^{\beta\alpha} & \mathbf{M}_{\Omega\mathrm{F}}^{\beta\beta} & \cdots & \mathbf{M}_{\Omega\mathrm{L}}^{\beta\alpha} & \mathbf{M}_{\Omega\mathrm{L}}^{\beta\beta} & \cdots & \mathbf{M}_{\Omega\mathrm{S}}^{\beta\alpha} & \mathbf{M}_{\Omega\mathrm{S}}^{\beta\beta} & \cdots \\ \vdots & \vdots & & \vdots & \vdots & & \vdots & \vdots & \\ \mathbf{M}_{\mathrm{EF}}^{\alpha\alpha} & \mathbf{M}_{\mathrm{EF}}^{\alpha\beta} & \cdots & \mathbf{M}_{\mathrm{EL}}^{\alpha\alpha} & \mathbf{M}_{\mathrm{EL}}^{\alpha\beta} & \cdots & \mathbf{M}_{\mathrm{ES}}^{\alpha\alpha} & \mathbf{M}_{\mathrm{ES}}^{\alpha\beta} & \cdots \\ \mathbf{M}_{\mathrm{EF}}^{\beta\alpha} & \mathbf{M}_{\mathrm{EF}}^{\beta\beta} & \cdots & \mathbf{M}_{\mathrm{EL}}^{\beta\alpha} & \mathbf{M}_{\mathrm{EL}}^{\beta\beta} & \cdots & \mathbf{M}_{\mathrm{ES}}^{\beta\alpha} & \mathbf{M}_{\mathrm{ES}}^{\beta\beta} & \cdots \\ \vdots & \vdots & & \vdots & \vdots & & \vdots & \vdots & \end{pmatrix} \cdot \begin{pmatrix} \mathbf{F}^{\alpha} \\ \mathbf{F}^{\beta} \\ \vdots \\ \mathbf{L}^{\alpha} \\ \mathbf{L}^{\beta} \\ \vdots \\ \mathbf{S}^{\alpha} \\ \mathbf{S}^{\beta} \\ \vdots \end{pmatrix}, \tag{1}$$

where superscripts α and β are particle labels, $\mathbf{U}^{\infty}$, Ω^{∞}, and $\mathbf{E}^{\infty}$ are respectively the far-field velocity, vorticity, and strain rate imposed at the center of the particle, and the matrix blocks such as $\mathbf{M}_{\mathrm{UF}}$ are the 3×3 mobility tensors. Each mobility tensor expresses the relationship between one of $\mathbf{U}$, Ω, $\mathbf{E}$, and one of $\mathbf{F}$, $\mathbf{L}$, $\mathbf{S}$ as indicated by the its subscripts. The superscripts indicate either self mobility, e.g., $\alpha\alpha$ for the effect of particle α on itself, or mutual mobility, e.g., $\alpha\beta$, for the effect of particle β on particle α. For free space (i.e., unbounded) flow, the mobility tensors in Eq. (1) can be found in many texts, e.g., Refs. [14,16]. In the presence of a no-slip wall, the mobility tensors have been derived in a previous work [13] for particles of different sizes. For example, the mobility tensor $M_{UF}^{\alpha\beta}$, which represents the effect on the velocity of particle α due to the force on particle β, is expressed by

$$\mathbf{M}_{\mathrm{UF}}^{\alpha\beta} = \frac{1}{8\pi\eta}\left(1+\frac{a_\alpha^2}{6}\nabla_{\mathbf{x}}^2\right)\left(1+\frac{a_\beta^2}{6}\nabla_{\mathbf{y}}^2\right)\mathbf{G}\Big|_{\substack{\mathbf{x}=\mathbf{x}^\alpha\\ \mathbf{y}=\mathbf{x}^\beta}}, \tag{2}$$

where G is Green's function for Stokes flow [17], a_α and a_β are the particle radii. The radii were set to be uniform in the previous Stokesian dynamics simulation of the flowable electrode [8]. In the present study, a_α and a_β could be different depending on whether the pair in the bimodal distribution consists of large–large, large–small, or small–small particles.

In the Stokesian dynamics, the hydrodynamic lubrication force between two particles in close proximity, or between one particle and the no-slip wall, is included into the resistance matrix, $\mathcal{R}$, which is the inverse of the mobility matrix, $\mathcal{M}$,

$$\mathcal{R} = (\mathcal{M}^\infty)^{-1} + \mathcal{R}_{\mathrm{2P}} + \mathcal{R}_{\mathrm{w}} - (\mathcal{R}_{\mathrm{2P}}^\infty + \mathcal{R}_{\mathrm{w}}^\infty), \tag{3}$$

where $\mathcal{M}^\infty$ is the far-field mobility matrix, $\mathcal{R}_{\mathrm{w}}$ and $\mathcal{R}_{\mathrm{2P}}$ are respectively the pairwise particle-wall and particle-particle lubrication resistance tensors [18]. These resistance tensors have been derived previously [19–23], and $\mathcal{R}_{\mathrm{w}}^\infty$ and $\mathcal{R}_{\mathrm{2P}}^\infty$ are respectively the pairwise far-field particle-wall and particle-particle resistance tensors that have been subtracted in Eq. (3) to avoid double counting.

It has been shown previously that the lubrication film can break down so there could be solid–solid contact interactions of both normal and tangential (frictional) forms [24,25]. However, due to a lack of experimental data available for the rough surface of the present particles, we limit ourselves to the hydrodynamic lubrication and define contact and the electrical resistance loosely based on the gap distance.

In the present study, we consider a simple shear flow with an average linear velocity profile of shear rate $\dot{\gamma}$. The flow is assumed to be periodic in the streamwise (x) direction. Thus, two additional periodic boxes around the simulation box with identical configuration of the particles are added on the left and right sides of the main box. The main simulation box has a dimension of L and H in the x- and z-directions. The effect of the particles in the periodic boxes has been included in the Stokesian dynamics formulation. To generate the flow, we place a row of the particles at the top of the box, whose translational velocity is equal to $\dot{\gamma}H$ and has zero rotational velocity.

2.2 A unified circuit model for particle charging

Consider a cluster of carbon particles in the slurry, some of which have pair contact with one another and some have contact with the stationary electrode. The electrical network can be approximated by the generalized circuit model shown in Fig. 2. In this circuit model, each carbon sphere is represented by a capacitor with capacitance C_i. The resistance due to ion diffusion into the pores is represented by a ground-connecting resistor R_{ei}. Any pair of two capacitors are connected by a resistor R_{ij} that represents the contact resistance between the two carbon spheres. When the two particles are separated, R_{ij} becomes infinite, and when the two particles are deemed in contact, R_{ij} takes a finite value that will be set later. In a similar way, the particle-wall contact is modeled as a resistor, R_{0i}, whose resistance becomes infinite when the two are separated.

To solve the generalized circuit in Fig. 2, we define the nodal potential before the capacitor, ϕ_i, and the potential at the node between the capacitor C_i and the ground-connecting resistor R_{ei}, ϕ_{ei}. The potential of the stationary electrode is ϕ_0. The electric current through the ith capacitor is I_i. Then, the charging dynamics of the capacitor can be written as

$$I_i = C_i\frac{\mathrm{d}(\phi_i-\phi_{ei})}{\mathrm{d}t} = \frac{\phi_{ei}}{R_{ei}}. \tag{4}$$

The current I_i is also a combination of the current feeds from all other capacitors and from the wall-charging potential, i.e.,

$$I_i = \frac{\phi_{ei}}{R_{ei}} = \frac{\phi_0-\phi_i}{R_{0i}} + \frac{\phi_1-\phi_i}{R_{1i}} + \frac{\phi_2-\phi_i}{R_{2i}} + \cdots \tag{5}$$

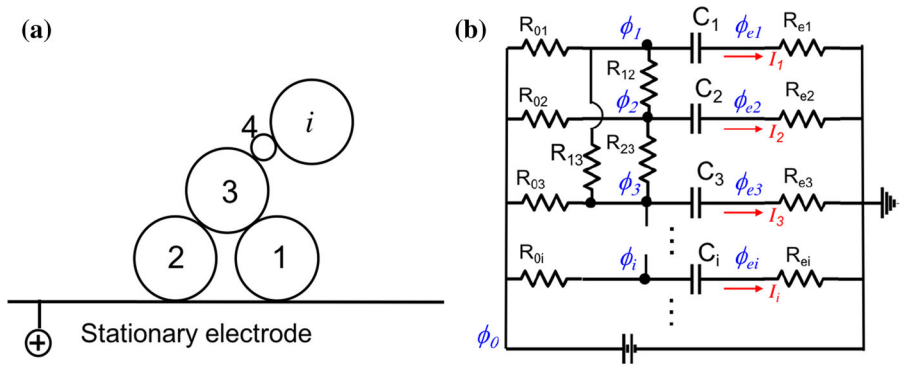

Fig. 2 **a** Schematic of carbon particles in contact with wall and with one another, and **b** generalized resistor-capacitor network model used to analyze the charging and discharging of particles

In order to solve the entire circuit, we define the potential across the capacitor, $\tilde{\phi}_i$, so that

$$\tilde{\phi}_i = \phi_i - \phi_{ei}. \tag{6}$$

Note that ϕ_i and ϕ_{ei} are not continuous in time and may experience jumps as the capacitor is disconnected or reconnected with other capacitors. Defining differential potential $\tilde{\phi}_i$, which is continuous in time, will thus facilitate the solution process.

Substituting Eqs. (6) into (5), we have

$$\frac{\phi_{ei}}{R_{ei}} = \sum_j \frac{\tilde{\phi}_j - \tilde{\phi}_i}{R_{ij}} + \sum_j \frac{\phi_{ej} - \phi_{ei}}{R_{ij}}, \qquad j = 0, 1, 2, \ldots, \; j \neq i, \tag{7}$$

where the charging potential ϕ_0 has been included in the formulation by assuming that $\phi_{e0} = 0$ and thus $\tilde{\phi}_0 = \phi_0$. Rearranging the equation, we obtain the linear equation system for ϕ_{ei},

$$\left(\frac{1}{R_{ei}} + \sum_j \frac{1}{R_{ij}}\right)\phi_{ei} - \sum_j \frac{\phi_{ej}}{R_{ij}} = \sum_j \frac{\tilde{\phi}_j - \tilde{\phi}_i}{R_{ij}}, \qquad j = 0, 1, 2, \ldots, \; j \neq i. \tag{8}$$

Equation (4) is re-written as

$$C_i \frac{d\tilde{\phi}_i}{dt} = \frac{\phi_{ei}}{R_{ei}}. \tag{9}$$

After replacing ϕ_{ei} and ϕ_{ej} in Eqs. (7) using (9), we obtain the equation system for charging of the capacitors,

$$\left(\frac{1}{R_{ei}} + \sum_j \frac{1}{R_{ij}}\right) R_{ei} C_i \frac{\mathrm{d}\tilde{\phi}_i}{\mathrm{d}t} - \sum_j \frac{R_{ej} C_j}{R_{ij}} \frac{\mathrm{d}\tilde{\phi}_j}{\mathrm{d}t} = \sum_j \frac{\tilde{\phi}_j - \tilde{\phi}_i}{R_{ij}}, \qquad j = 0, 1, 2, \ldots, \; j \neq i. \tag{10}$$

To include $j = 0$ in this index notation, we simply assume that $C_0 = 0$. Note that we use the potential difference $\tilde{\phi}_i$, instead of ϕ_i, as the solution variable since the potential difference and the charge of each particle, $Q_i = C_i \tilde{\phi}_i$, are continuous in time.

Equation (10) can be re-written in the matrix form as below

$$\left(\mathbf{R_e}^{-1} - \mathbf{B}\right)\mathbf{R_e}\mathbf{C}\frac{\mathrm{d}\tilde{\boldsymbol{\phi}}}{\mathrm{d}t} = \mathbf{B}\tilde{\boldsymbol{\phi}} + \phi_0 \mathbf{b_0} \tag{11}$$

where

$$\tilde{\boldsymbol{\phi}} = \begin{bmatrix} \tilde{\phi}_1 \\ \tilde{\phi}_2 \\ \tilde{\phi}_3 \\ \cdots \end{bmatrix}, \quad \mathbf{R_e} = \begin{bmatrix} R_{e1} & & & \\ & R_{e2} & & \\ & & R_{e3} & \\ & & & \cdots \end{bmatrix}, \quad \mathbf{C} = \begin{bmatrix} C_1 & & & \\ & C_2 & & \\ & & C_3 & \\ & & & \cdots \end{bmatrix},$$

$$\mathbf{B} = \begin{bmatrix} -\sum_j \frac{1}{R_{1j}} & \frac{1}{R_{12}} & \frac{1}{R_{13}} & \cdots \\ \frac{1}{R_{21}} & -\sum_j \frac{1}{R_{2j}} & \frac{1}{R_{23}} & \cdots \\ \frac{1}{R_{31}} & \frac{1}{R_{32}} & -\sum_j \frac{1}{R_{3j}} & \cdots \\ \cdots & \cdots & \cdots & \cdots \end{bmatrix}, \quad \mathbf{b_0} = \begin{bmatrix} \frac{1}{R_{01}} \\ \frac{1}{R_{02}} \\ \frac{1}{R_{03}} \\ \cdots \end{bmatrix}. \tag{12}$$

In practice, the intermediate potential $\boldsymbol{\phi_e}$ can be first solved from Eq. (8) at a given time step; then, the potential difference $\tilde{\boldsymbol{\phi}}$ can be advanced directly from Eq. (9).

When the slurry is flowing, the instantaneous configuration of the particle network evolves with time. Particle–particle and particle–wall contacts may be broken when the contact pair are separated. However, the unified equation system in Eq. (11) still holds, as one only needs to modify the instantaneous resistance of the resistors. In practice, we set a nominal resistance value for zero gap distance and use a function to express its dependence on the gap distance between the two particles as well as their radii. The resistance is set to infinity when the gap distance reaches 10% of the particle radius for an equal-size pair as described in a previous study [8]. This threshold is based on the assumption of the surface roughness, ϵ, at 5% of the particle radius and a contact model that calculates a radius of the contact area, r_c, and the contact resistance R_{ij}. This resistance model is somewhat arbitrary as there is no direct experimental data available. On the other hand, the effect of the gap threshold, and thus the contact resistance, can be grouped along with the capacitance C_i into the charging timescale, $\tau_e = (R_{ij} + R_{ei})C_i$, whose significance has been discussed previously [8]. In this study, we will keep the charging time scale constant and will focus on the effect of bimodal distribution.

Equations (8) and (9) can be solved iteratively for any given time step. The particles are initially uncharged before entering the domain, i.e., $Q_i = \tilde{\phi}_i = 0$. In the current study, we use the Crank–Nicholson implicit scheme to discretize the time derivatives and employ the Gauss–Seidel method to iterate the system at a given time step until convergence is reached with a maximum allowable error at 10^{-6} of the constant wall potential ϕ_0. Here a Gauss–Siedel model was chosen for simplicity, as the solution converges fairly quickly. For reference, a typical timestep takes less than 0.5 seconds for 50 particles (25 large and 25 small), and the charge model calculations take only a small fraction of this time. For the bimodal distribution, the small particles are treated in the same way as the large particles, except that their capacitance is very small and they get nearly instantly charged if they are in contact with a charged surface of a large particle or the wall. Therefore, the primary function of the small particles in the circuit is to provide additional connecting branches, which corresponds to the function of the conductive additive in the actual slurry electrode.

The hydrodynamic simulation has been verified against previous Stokesian dynamics work and also against a boundary-element method (BEM) [26], as explained in Karzar-Jeddi et al. [13]. For further verification, we have performed more BEM simulations to test our code at the current particle size ratio (see Appendix A). The new charging model is also verified using a Matlab® code for configurations of only a few particles.

3 Simulation setup

The simulation domain as shown in Fig. 3 represents a slice of the charging domain of an EFC. In this study, we use $N_a = 25$ uniform activated carbon particles for fast simulations, which are assumed to have the same capacitance C, and ground resistance R_e. N_b is the number of carbon black particles to be varied in the study. The size of the domain is adjusted according to the specified volume concentration of the particles, φ. The flow is driven by the top row particles shown in Fig. 3 whose translation is specified. The imposed shear rate, $\dot{\gamma}$, provides a time scale for the hydrodynamics, which is defined as $\tau_h = \dot{\gamma}^{-1}$. The time scale of particle charging is defined as $\tau_e = (R_C + R_e)C$, where R_c is the contact resistance of two large particles when the gap is zero. In this problem, we set $\tau_h/\tau_e = 1$ and will focus on the effect of adding different numbers of carbon black particles at different volume concentrations. The effect of the time-scale ratio, τ_h/τ_e, was considered in the previous study [8].

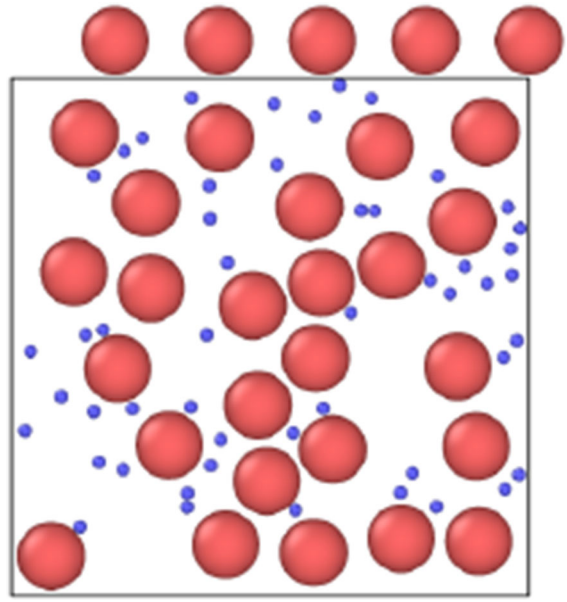

Fig. 3 An example of the initial positions of the particles in the simulation. Here the red spheres are the $N_a = 25$ activated carbon particles, and the blue spheres are the $N_b = 50$ carbon black particles. (Color figure online)

The small particles are randomly added to the void space between the large particles. We set the radius of the small particles to be 1/5th of the radius of the large particles using the structure size ranges established by the International Carbon Black Association User Guide for carbon black aggregates. According to this reference, while individual carbon black particles are between 10 and 300 nm, distinct carbon black particles do not typically exist due to bonding between the particles to form aggregates. These aggregates can be sized between 85 and 500 nm. Given that the activated carbon particles are on the order of 1 to 10 μm for flowable electrodes, the ratio of 1/5th for the radii was deemed appropriate. We consider three volume concentrations that are defined using the volume of the large particles, $\varphi = 0.10$, 0.15, and 0.20. For each volume concentration, three cases are simulated: no carbon black ($N_b = 0$), $N_b = 25$, and $N_b = 50$.

To start off the simulation, the initial positions of the particles are determined by randomly placing them inside of the simulation domain, while ensuring there is no overlap. An example is shown in Fig. 3 for $\varphi = 0.15$ with 25 large activated carbon particles and 50 carbon black particles. The new position of the particles are integrated using a 4th-order Runge–Kutta scheme. At each integration step, the linear equation system of the Stokesian dynamics is solved to obtain the velocity of the particles. The time step size is kept at $\Delta t = 0.005\dot{\gamma}^{-1}$ to avoid particle overlapping during interaction. Each simulation is run for at least 20,000 steps. The first 2000 steps are not included when calculating the average charge contours, so that the flow is able to fully develop from the initial condition.

Since the carbon black does not have a large interior porous surface like activated carbon, the capacitance of the small particles is set to be much smaller as compared with the large particles. In addition, the nominal resistance between a large particle and a small particle is 2.5 times of that between two large particles.

4 Results and discussions

For each volume concentration and particle composition, we run five simulations and average the electrical charge contours in the domain. During each individual simulation, the particles at the top of the computational domain pass through the domain over 100 times. This allows many particle interactions to happen and for the statistics to converge, so the five simulations are averaged only to further smooth the results. More simulations do not significantly change the results, as shown by a comparison in Appendix A. In order to compute the contours, the computational box is divided into 15×7 smaller blocks centered at (x_i, y_j). The charge level of each block is computed by averaging the charge carried by the particles located within the block:

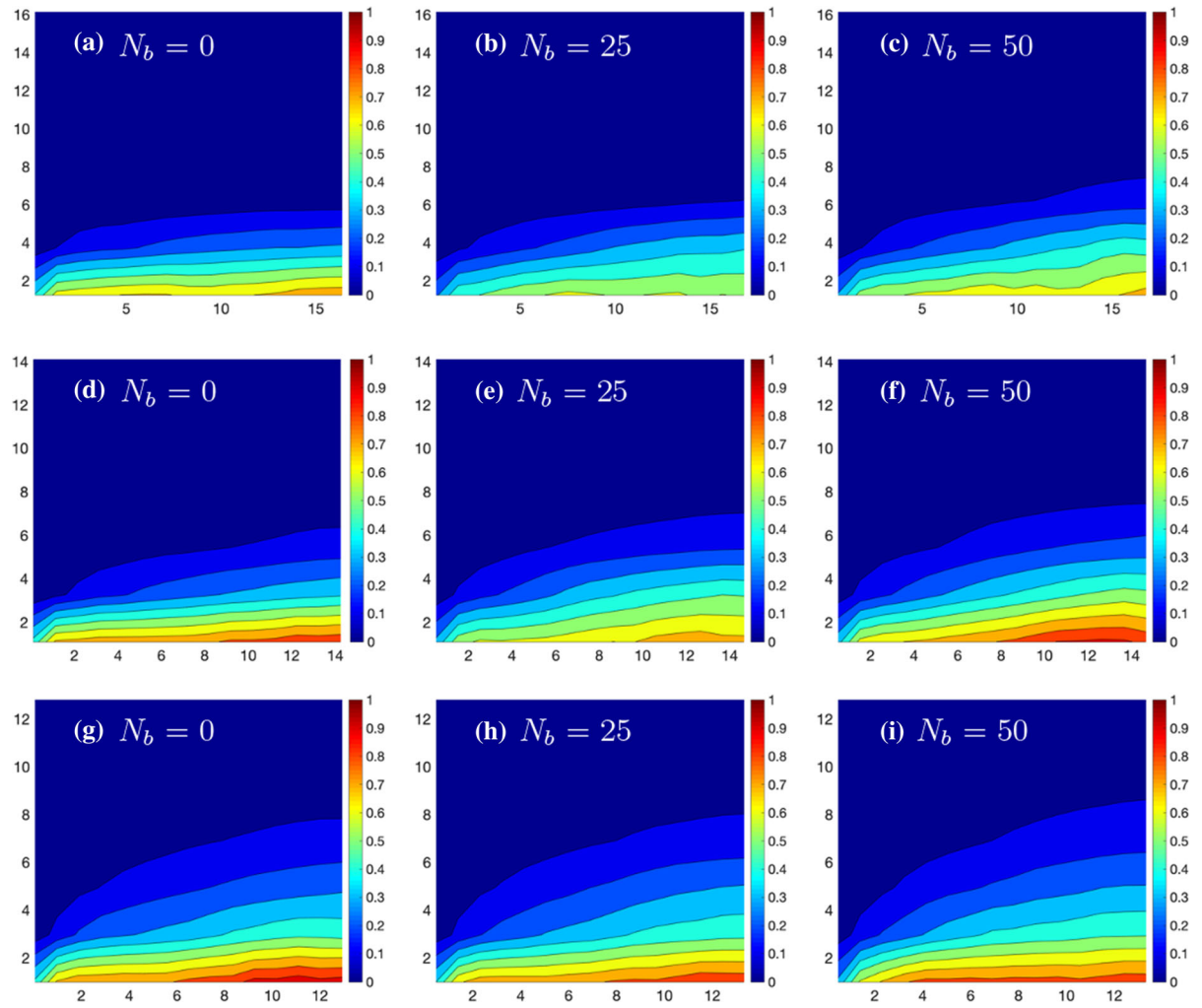

Fig. 4 Time-averaged charge contour, $\langle Q(x, y)\rangle$, from simulations with a volume concentration of $\varphi = 0.10$ (**a**–**c**), $\varphi = 0.15$ (**d**–**f**), and $\varphi = 0.20$ (**g**–**i**). From left to right, the number of carbon black particles is $N_b = 0$, $N_b = 25$, $N_b = 50$

$$\langle Q(x_i, y_j)\rangle = \frac{\int_0^T \sum_{k=1}^{n(t)} C_k \phi_k \, \mathrm{d}t}{\Delta x_i \Delta y_j n_0 C_0 \phi_0 T}, \tag{13}$$

where charge $\langle Q(x_i, y_j)\rangle$ is the time-averaged electrical charge at the block (x_i, y_j) and is normalized by the average charge of the entire domain, T is the total computation time, $n(t)$ is number of large particles within the block at time t, $\tilde{\phi}_k$ is the potential difference of particle k at time t, C_k is the particle's capacitance, Δx_i and Δy_j are the sizes of the block, n_0 is the average number density of large particles in computational domain, and C_0 is the capacitance of the large particles. The small particles carry negligible amount of charge and thus are not included in this calculation.

The results from the simulations are presented in Fig. 4, where the charge contour plots have been organized from lowest to highest volume concentration from the top to the bottom. The left column, Fig. 4a, d, and g are simulations that do not contain any carbon black particles ($N_b = 0$), Fig. 4b, e, and h are simulations that contain $N_b = 25$ carbon black particles, and Fig. 4c, f, and i are simulations that contain $N_b = 50$ carbon black particles. It should be noted that the results near the wall in the contours are difficult to converge, as the particles there are slow moving while being fully charged. Therefore, the average charge in these areas may appear to be better with

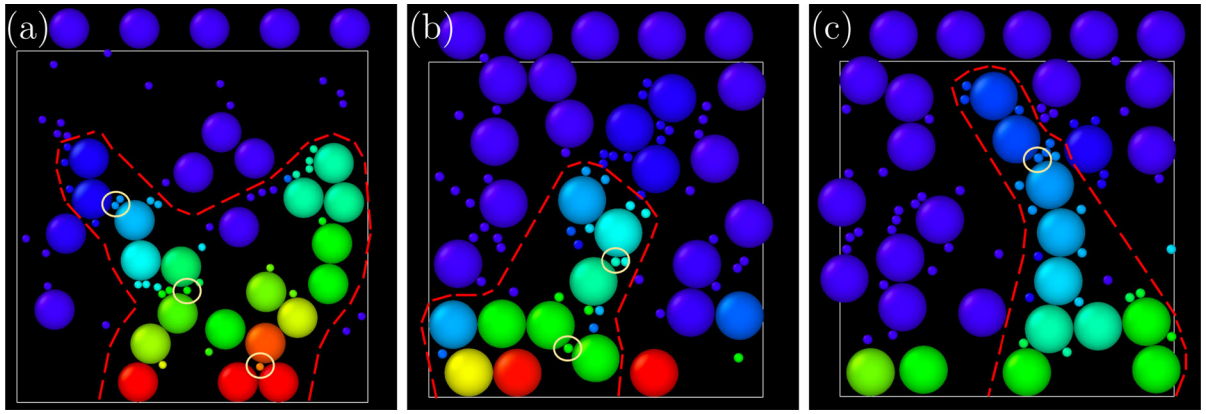

Fig. 5 **a** A snapshot of the particles from the simulation with $\varphi = 0.10$ and $N_b = 50$. **b**, **c** Two snapshots of the particles from the simulation with $\varphi = 0.20$ and $N_b = 50$. The red lines trace a charging cluster, and the yellow circles surround the carbon black particles that allow more activated carbon particles to join the cluster. (Color figure online)

fewer carbon black particles; however, the contours should be viewed as a whole in order to see how the carbon black particles affect the charge of the entire simulation domain.

These plots display two trends that occur when the carbon black particles are included in the simulation domain. Firstly, at the two low concentration levels, $\varphi = 0.10$ and 0.15, the charge from the stationary electrode at the bottom is able to penetrate deeper into the bulk slurry as the number of the carbon black particles is increased from zero to 25 and then to 50. This result suggests that the carbon black is playing a positive role in the charge transfer. Secondly, at the higher volume concentration of $\varphi = 0.20$, the charge depth inside the bulk slurry is only slightly improved with the increase of the carbon black. Therefore, the result suggests that the bonus effects of adding the smaller particles are reduced at the higher concentration.

To further investigate the effect of the carbon black particles, we examined qualitatively the cluster behavior within the moving slurry by inspecting the particle motion from the animations. As seen from a snapshot of the particles in Fig. 5a, where the concentration is $\varphi = 0.10$, the small particles may get into the interstitial space between the large particles, thus serving as conducting bridges and increasing the chances of charge transfer among the large particles. Without the small particles, some of the particles in the cluster shown in the figure would not otherwise receive the charge. Under this effect, higher numbers of carbon black particles intensify the charge transfer among the large particles and create an overall better charging network. This result is consistent with the expectation that the carbon black particles are meant to increase the number of particle interactions, while the activated carbon particles play the dominant role in charge storage.

On the other hand, if the volume concentration is high, the carbon black particles can still serve as connecting bridges as seen in Fig. 5b. However, more often they become located away from large particles, rather than being trapped between them. This effect is shown in Fig. 5c. In this case, the carbon black particles cannot produce helpful results to the charging network if there is limited interstitial space for the particles to enter. Instead, the particle interactions are dominated by those among the large particles themselves, and adding small particles may not necessarily lead to significant improvement.

Adding small particles to the slurry may affect the apparent viscosity of the slurry, an effect that is not discussed in this work but has been studied in the context of rheology of colloids and suspensions [27–30]. In the light of those studies, a further investigation for the slurry electrode could look into the effect of the carbon black on the characteristics of the particle clusters, e.g., cluster size and pair distribution [16], or the optimal fraction of the carbon black that may balance the charge transfer performance and the viscosity of the slurry. However, the current work is meant to introduce the mathematical framework and to illustrate its use in an exploratory study. We defer those topics to a future study.

5 Conclusion and further remarks

We have developed a computational model that couples the particle hydrodynamics and the electrical charge transfer inside a flowable slurry electrode. A unified expression for the topology-varying electrical network consisting of the moving carbon particles has been created to address the charge transfer among the particles. Here we expand upon previous work, where only the activated carbon particles were simulated [8], and incorporate the effect of the conducting additive by modeling a bimodal distribution of particles. Thus, the current work provides a more detailed picture into how the hydrodynamic interactions among the particles may effectively distribute the charge from the stationary electrode. Our results suggest that at lower concentrations, the additive particles lead to significant improvement on the charge transfer across the slurry flow; at higher concentrations, however, particle interactions could be dominated by direct contact of the large particles, and thus, the small particles may have a limited effect on the charge transfer.

The present simulations are meant to provide a small-window view into the fundamental mechanisms at work inside the flowable electrodes. We envision that this type of model will be used in the future to study the coupling between the hydrodynamics and charge transfer process in such electrodes. We are currently designing single-particle experiments to study a small number of particles and directly observe their interactions. The present computational model will provide a complementary tool for those experimental studies. Furthermore, we aim to scale up the simulation by incorporating parallel computing and algorithm optimization to simulate many more particles, possibly incorporating size distributions, so that the simulations will find more practical use in the design of the EFC and similar systems.

Acknowledgements This work was supported by an NSF Grant (CBET-1921320). Prof. Kelsey B. Hatzell's help in this work is gratefully acknowledged.

Appendix A

In addition to the verification in Karzar-Jeddi et al. [13], we have done further tests of the SD code against the BEM calculations using a code previously developed by Prof. Pozrikidis [26]. In this test, the particle ratio $a_2/a_1 = 5$ is used to match the bimodal particle interactions in the present SD simulation. A total of 1294 triangular elements with 7 Gaussian integration points (6 integration points for singular elements) were used in the BEM for each particle.

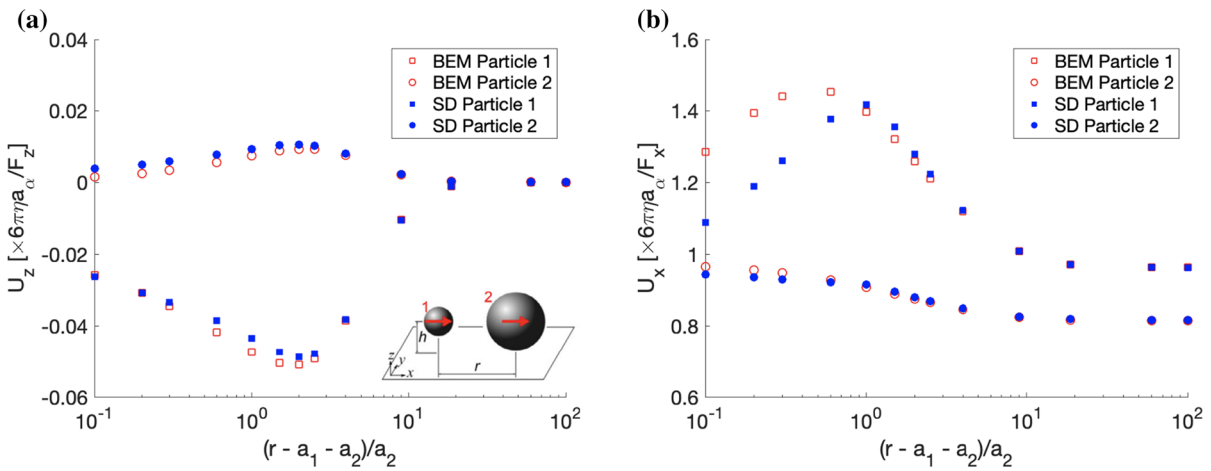

Fig. 6 Test of the present SD code against a BEM code [26]. Normalized wall-normal (**a**) and inline (**b**) particle velocities plotted against the normalized gap distance. The size ratio for the particles is $a_2/a_1 = 5$, and the distance from the center of the particles to the wall is $h = 3a_2$

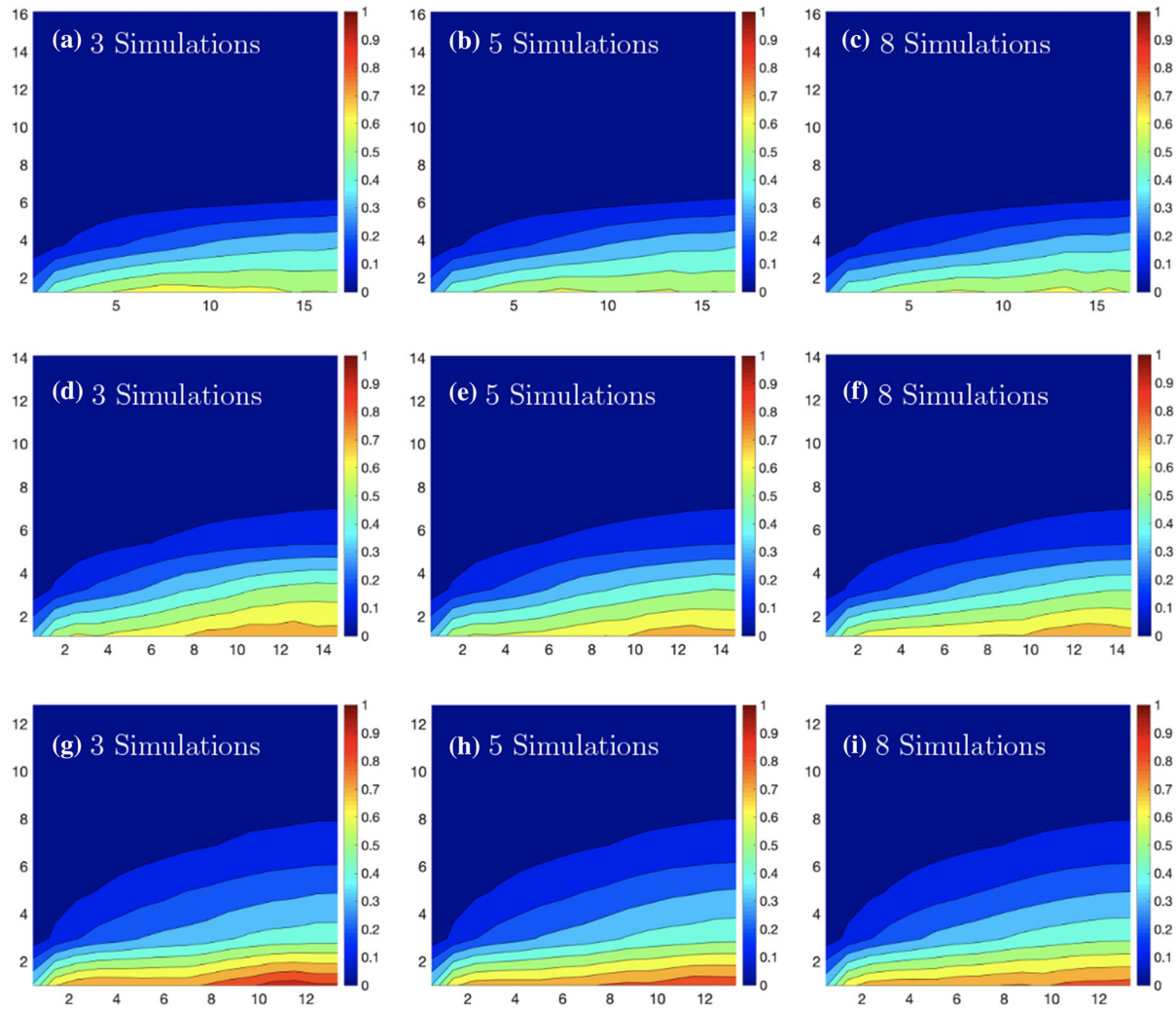

Fig. 7 Time-averaged charge contour, $\langle Q(x, y)\rangle$, averaged from up to 8 simulations for each case. Here, the volume concentration is $\varphi = 0.10$ (**a**–**c**), $\varphi = 0.15$ (**d**–**f**), and $\varphi = 0.20$ (**g**–**i**)

Figure 6a displays the normalized wall-normal particle velocity versus the normalized gap distance between the two particles, while Fig. 6b displays the inline particle velocity. The calculations from the SD simulation we employ agree well with the BEM method, especially at a gap distance greater than a_2. At lower gaps, the inline velocity shows more pronounced differences for the smaller particle, but the error is still within 15%. Similar to Karzar-Jeddi et al. [13], further mesh refinement in the BEM shows that this discrepancy persists. Thus, the lubrication approximation in the Stokesian dynamics likely has caused the error.

In order to verify the statistical results, a comparison of three, five, and eight simulations was performed on the $N_b = 25$ case for the three volume concentrations. This comparison, as seen in Fig. 7, shows that the charge contours are consistent among these calculations and thus ensures that the number of simulations used to provide the data for Fig. 4 is sufficient.

References

1. Presser V, Dennison CR, Campos J, Knehr KW, Kumbur EC, Gogotsi Y (2012) The electrochemical flow capacitor: a new concept for rapid energy storage and recovery. Adv Energy Mater 2(7):895–902
2. Dennison CR, Beidaghi M, Hatzell KB, Campos JW, Gogotsi Y, Kumbur EC (2014) Effects of flow cell design on charge percolation and storage in the carbon slurry electrodes of electrochemical flow capacitors. J Power Sources 247:489–496
3. Hatzell KB, Boota M, Gogotsi Y (2015) Materials for suspension (semi-solid) electrodes for energy and water technologies. Chem Soc Rev 44(23):8664–8687
4. Si Jeon, Hr Park, Jg Yeo, Yang S, Cho CH, Han MH, Kim DK (2013) Desalination via a new membrane capacitive deionization process utilizing flow-electrodes. Energ Environ Sci 6(5):1471
5. Suss ME, Porada S, Sun X, Biesheuvel PM, Yoon J, Presser V (2015) Water desalination via capacitive deionization: what is it and what can we expect from it? Energy Environ Sci 8(8):2296–2319
6. Hoyt NC, Wainright JS, Savinell RF (2015a) Mathematical modeling of electrochemical flow capacitors. J Electrochem Soc 162(4):A652–A657
7. Hoyt NC, Wainright JS, Savinell RF (2015b) Current density scaling in electrochemical flow capacitors. J Electrochem Soc 162(6):A1102–A1110
8. Karzar-Jeddi M, Luo H, Cummings PT, Hatzell KB (2019) Computational modeling of particle hydrodynamics and charging process for the flowable electrodes of carbon slurry. J Electrochem Soc 166(12):A2643–A2653
9. Kirk TL, Evans J, Please CP, Chapman SJ (2020) Modelling electrode heterogeneity in lithium-ion batteries: unimodal and bimodal particle-size distributions. arXiv preprint arXiv:2006.12208
10. Marquis SG, Timms R, Sulzer V, Please CP, Chapman SJ (2020) A suite of reduced-order models of a single-layer lithium-ion pouch cell. J Electrochem Soc 167(14):140513
11. Brady JF, Bossis G (1985) The rheology of concentrated suspensions of spheres in simple shear flow by numerical simulation. J Fluid Mech 155:105
12. Brady JF, Morris JF (1997) Microstructure of strongly sheared suspensions and its impact on rheology and diffusion. J Fluid Mech 348:S0022112097006320
13. Karzar-Jeddi M, Luo H, Cummings PT (2018) Mobilities of polydisperse hard spheres near a no-slip wall. Comput Fluids 176:40–50
14. Durlofsky L, Brady JF, Bossis G (1987) Dynamic simulation of hydrodynamically interacting particles. J Fluid Mech 180(1987):21–49
15. Brady JF, Bossis G (1988) Stokesian dynamics. Annu Rev Fluid Mech 20(1):111–157
16. Chang C, Powell RL (1993) Dynamic simulation of bimodal suspensions of hydrodynamically interacting spherical particles. J Fluid Mech 253:1–25
17. Pozrikidis C (1992) Boundary integral and singularity methods for linearized viscous flow. Cambridge University Press, Cambridge
18. Swan JW, Brady JF (2007) Simulation of hydrodynamically interacting particles near a no-slip boundary. Phys Fluids 19(11):113306
19. Corless RM, Jeffrey DJ (1988) Stress moments of nearly touching spheres in low Reynolds number flow. Zeitschrift für angewandte Mathematik und Physik ZAMP 39(6):874–884
20. Jeffrey D, Corless R (1988) Forces and stresslets for the axisymmetric motion of nearly touching unequal spheres. PhysicoChem Hydrodyn 10(4):461–470
21. Jeffrey DJ, Onishi Y (1984) Calculation of the resistance and mobility functions for two unequal rigid spheres in low-Reynolds-number flow. J Fluid Mech 139(1):261–290
22. Cooley MDA, O'Neill ME (1969) On the slow motion generated in a viscous fluid by the approach of a sphere to a plane wall or stationary sphere. Mathematika 16(01):37
23. Goldman A, Cox R, Brenner H (1967) Slow viscous motion of a sphere parallel to a plane wall-II Couette flow. Chem Eng Sci 22(4):653–660
24. Singh A, Mari R, Denn MM, Morris JF (2018) A constitutive model for simple shear of dense frictional suspensions. J Rheol 62(2):457–468
25. Wyart M, Cates M (2014) Discontinuous shear thickening without inertia in dense non-brownian suspensions. Phys Rev Lett 112(9):098302
26. Pozrikidis C (2002) A practical guide to boundary element methods with the software library BEMLIB. CRC Press, Boca Raton
27. Chang C, Powell RL (1994) The rheology of bimodal hard-sphere dispersions. Phys Fluids 6(5):1628–1636
28. Farris R (1968) Prediction of the viscosity of multimodal suspensions from unimodal viscosity data. Trans Soc Rheol 12(2):281–301
29. Shapiro AP, Probstein RF (1992) Random packings of spheres and fluidity limits of monodisperse and bidisperse suspensions. Phys Rev Lett 68(9):1422
30. Pednekar S, Chun J, Morris JF (2018) Bidisperse and polydisperse suspension rheology at large solid fraction. J Rheol 62(2):513–526